Journal of Electronic Research and Application, 2026, Volume 10, Issue 7
http://ojs.bbwpublisher.com/index.php/JERA
Online ISSN: 2208-3510
Print ISSN: 2208-3502

Simulation Study on the Crashworthiness of a Bridge Crane Anti-Collision Mechanism

Wenzhe Yan*, Yufei Yan, Siqun Ma

Zhan Tianyou College of Dalian Jiaotong University (CRRC College), Dalian 116028, Liaoning, China

***Corresponding author:** Wenzhe Yan, 19741197730@163.com

Abstract: A bridge-crane trolley may strike the end anti-collision device after overtravel, braking failure, or control delay; therefore, the collision resistance of the device directly affects operational safety. In this study, a shell-based finite-element model of a bridge-crane anti-collision mechanism was developed in HyperMesh, and explicit impact simulations were conducted in LS-DYNA at trolley speeds of 25 and 35 m/min. Each simulation covered 80 ms, and sliding energy, hourglass energy, added mass, stress, and displacement were examined. The sliding- and hourglass-energy ratios remained below 5%, and the added mass stayed below 1% in both cases. At 25 m/min, the maximum von Mises stress was 342.294 MPa, slightly below the 345 MPa yield strength of Q345 steel. At 35 m/min, the maximum stress increased to 429.190 MPa and exceeded the yield strength. These findings provide a basis for strength verification, end-zone speed limitation, and structural improvement of bridge-crane anti-collision mechanisms.

Keywords: Bridge crane; Anti-collision mechanism; Impact response; Crashworthiness

Online publication: Aug 11, 2026

1. Introduction

Bridge cranes perform frequent material-handling operations in workshops, warehouses, and metallurgical plants. Near the end of trolley travel, positioning error, insufficient braking distance, or payload swing may impose an unintended impact on the protective device. Sliding-mode control based on an improved nonlinear reaching law has been used to improve positioning and suppress payload swing in bridge cranes [1]. Model tests on lightweight bridge-crane girders also show that structural strength and static stiffness still require mechanical analysis and experimental verification [2]. Active control reduces collision probability, but it cannot cover every sensor fault, operator error, or brake failure; the mechanical end device therefore remains the final protective barrier.

An end impact is short and involves rapidly changing contact conditions, so a conventional static check cannot reproduce the transient load path. Zhao et al. showed through an energy-absorbing bumper study that multipoint collision and buffer deformation alter the attenuation of impact energy [3]. This finding indicates that an anti-collision mechanism should not be assessed from a single stress peak alone; energy conversion, velocity rebound, and local deformation should also be reviewed.

For beam-like and thin-walled absorbers, cross-sectional geometry, wall thickness, and material yielding jointly affect the impact-force peak and energy-absorption efficiency. Reduced-integration shell elements may also exhibit zero-energy modes; without checks on hourglass energy and total-energy balance, a local contour peak can be magnified by numerical artifacts. Crashworthiness evaluation should therefore examine structural response and numerical quality together.

Accordingly, the present work evaluates an existing bridge-crane anti-collision mechanism under two trolley-speed levels. The study addresses three engineering questions: whether the energy response of the numerical model is reliable, whether yielding occurs at 25 or 35 m/min, and how the stress, velocity, and displacement histories can guide speed limitation and local reinforcement.

2. Structure and finite-element model

2.1. Geometry processing and meshing

The geometry of the crane bridge and end anti-collision mechanism was exported from SolidWorks as a STEP file and imported into HyperMesh. Free edges, duplicate surfaces, and local discontinuities were corrected before midsurfaces were extracted from the plate components. The anti-collision mechanism consists mainly of a base, vertical plate, side plates, and connecting plates. Because impact force is transmitted from the contact plate toward the supports and bridge girders, the geometric details around the contact zone and plate junctions were retained.

Four-node shell elements were used. Element sizes of 8, 10, 12, 18, and 30 mm were assigned according to plate thickness and local geometric scale. Symmetric regions were generated by reflection, after which coincident nodes were equivalenced. The final model contained 106,516 elements. Aspect ratio, warpage, Jacobian, and edge length were checked before solution. The completed mesh is shown in **Figure 1**. Orthogonal hourglass control was applied to the reduced-integration elements to suppress nonphysical zero-energy deformation. Belytschko et al. showed that orthogonal hourglass stabilization can suppress zero-energy modes while preserving the consistency of under-integrated finite-element equations [4].

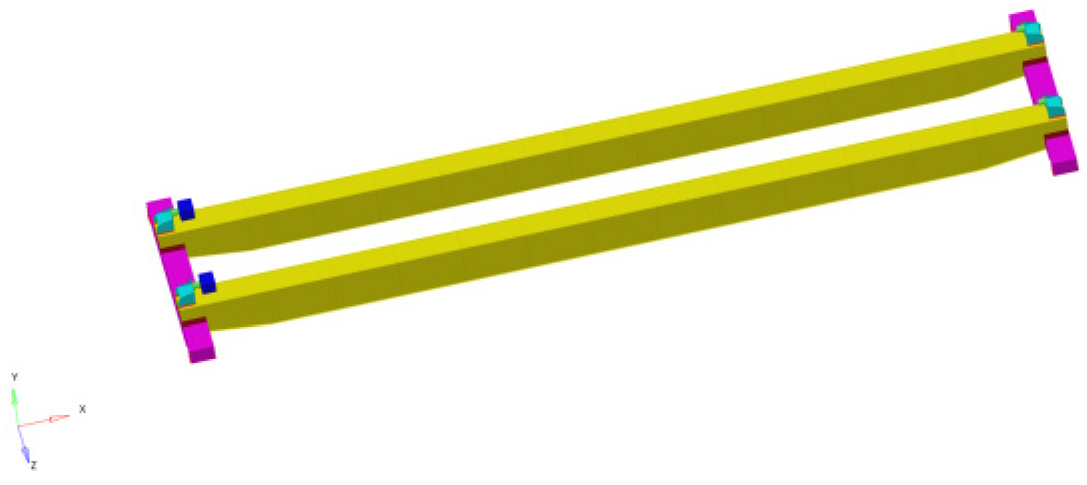

Figure 1. Finite-element mesh of the bridge crane.

2.2. Material, loading, contact, and constraints

The crane bridge and anti-collision mechanism were modeled as Q345 steel using the *MAT_024 piecewise-linear plasticity model. In the tonne-mm-ms unit system, the density was 7.800×10^{9}, Young's modulus was 210,000 MPa, Poisson's ratio was 0.30, and the yield strength was 345 MPa. Shell-section properties were assigned separately to each thickness group so that the midsurface model retained the mass and bending-stiffness characteristics of the physical structure. Hambali et al. compared six bumper-beam materials using impact toughness, flexural strength, and related criteria, supporting simultaneous consideration of energy absorption and load capacity [5].

The trolley and lifting assembly were replaced by a rigid impactor with an equivalent weight of 14,700 N. Initial velocity was applied in the negative X direction at 416.67 mm/s (25 m/min) and 583.33 mm/s (35 m/min). The simulation duration was 80 ms in both cases. The initial impact kinetic energy was calculated using Eq. (1). The impact load and rigid-impactor setup are shown in **Figure 2**.

$$E_{k0} = \frac{1}{2} m v_0^2 \tag{1}$$

where E_{k0} is the initial kinetic energy of the equivalent rigid system, m is the equivalent mass of the trolley and lifting assembly, and v_0 is the initial velocity along the impact direction.

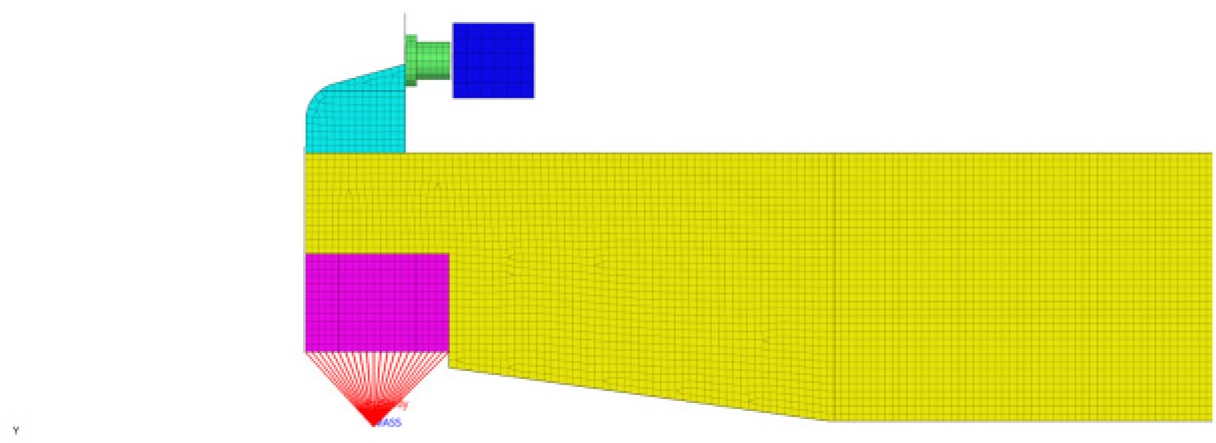

Figure 2. Impact load and rigid-impactor setup.

Boundary conditions included gravity, support constraints, and contact. Nodes in the lower support region were coupled to a reference mass point through rigid links, and the corresponding degrees of freedom were constrained, as shown in **Figure 3**. Automatic surface-to-surface contact was defined between the rigid impactor and the anti-collision mechanism, while automatic single-surface contact was applied to the deformable structure. Both static and dynamic friction coefficients were set to 0.2.

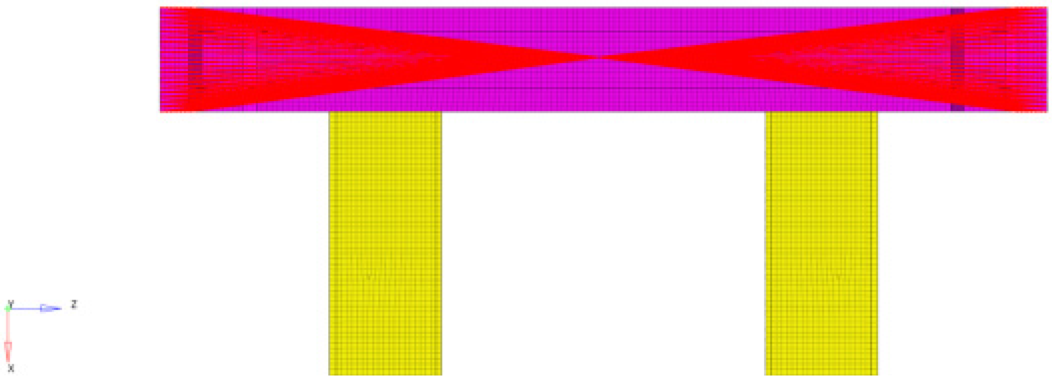

Figure 3. Constraints in the bridge-support region.

The impactor used *MAT_020, whereas the deformable components used *MAT_024. This idealization preserved the impacting mass, velocity, contact zone, and dominant load path without introducing trolley details unrelated to the objective.

3. Simulation evaluation indices

Energy balance was examined before interpreting the structural response. When minor dissipative terms are neglected, the total system energy can be approximated by Eq. (2). A stable total-energy history, together with the expected transfer from kinetic energy to internal energy, indicates a physically reasonable global energy path.

$$E_{total} \approx E_k + E_{int} + E_{sl} + E_{hg} \tag{2}$$

where E_{total} is total system energy, E_k is kinetic energy, E_{int} is structural internal energy, E_{sl} is sliding (interface) energy, and E_{hg} is hourglass energy.

The sliding- and hourglass-energy ratios were calculated using Eq. (3) to quantify the influence of contact and reduced integration. Olovsson et al. showed that selective mass scaling can increase the critical time step of an explicit analysis by modifying high-frequency response, provided that the low-frequency structural behavior is not materially altered [6]. Accordingly, a review threshold of 5% was used for both energy ratios, and the added mass produced by mass scaling was checked simultaneously.

$$\eta_{sl} = \frac{E_{sl}}{E_{total}} \times 100\%, \quad \eta_{hg} = \frac{E_{hg}}{E_{total}} \times 100\% \tag{3}$$

where η_{sl} and η_{hg} are the percentages of sliding and hourglass energy relative to total energy, respectively; E_{sl}, E_{hg}, and E_{total} have the meanings defined for Eq. (2).

Structural strength was evaluated using the von Mises equivalent stress expressed by Eq. (4). The X-velocity history and X-displacement of a node near the impact zone were also extracted to identify deceleration, rebound, and local deformation stages.

$$\sigma_{vm} = \sqrt{\frac{\left(\sigma_1\sigma_2\right)^2 + \left(\sigma_2\sigma_3\right)^2 + \left(\sigma_3\sigma_1\right)^2}{2}} \tag{4}$$

where σ_{vm} is the von Mises equivalent stress and σ_1, σ_2, and σ_3 are the first, second, and third principal stresses at the material point.

The maximum equivalent stress was compared with the Q345 yield strength. Stress margin and safety factor were obtained from Eq. (5) to distinguish a below-yield response from local plasticity.

$$S = \frac{\sigma_y - \sigma_{max}}{\sigma_y} \times 100\%, \quad n = \frac{\sigma_y}{\sigma_{max}} \tag{5}$$

where S is the stress margin relative to yield strength, n is the safety factor, σ_y is the material yield strength, and σ_{max} is the maximum von Mises stress from the simulation. Values of $S > 0$ and $n > 1$ indicate that the peak stress remains below yield.

4. Results and discussion

4.1. Energy conversion and numerical stability

The energy histories for both speeds are presented in **Figure 4**. After contact begins, rigid-body kinetic energy decreases continuously while the internal energy of the anti-collision structure increases. A modest recovery in kinetic energy then appears as stored structural energy is released and the trolley rebounds. No sudden jump or sustained drift is observed in the total energy over 80 ms, indicating a stable global energy-conversion process.

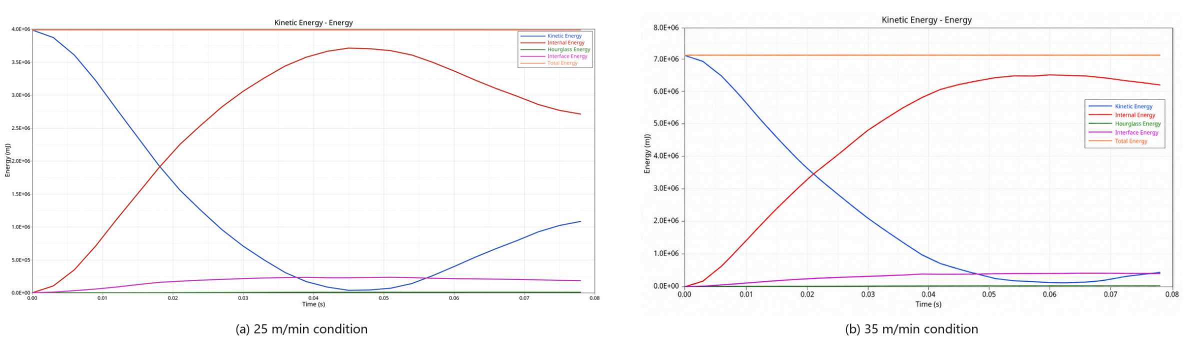

Figure 4. Energy histories at the two impact speeds.

At the end of the 25 m/min analysis, sliding energy was 184,176 mJ and total energy was 3,984,880 mJ, giving a ratio of 4.7%. Hourglass energy was 7,754 mJ, or 0.19% of total energy. At 35 m/min, sliding energy and total energy were 353,179 and 7,078,580 mJ, respectively, yielding a ratio of 4.9%; hourglass energy was 26,004 mJ, or 0.37%. Both ratios remained below 5%, so neither contact artifacts nor hourglass deformation governed the response.

As shown in **Figure 5**, the maximum added mass was approximately 0.97% at 25 m/min and 0.98% at 35 m/min. These values are well below 5%, demonstrating that the time-step control did not obtain efficiency through excessive artificial mass. The combined energy and mass-scaling checks provide an acceptable numerical basis for comparing stress, velocity, and displacement.

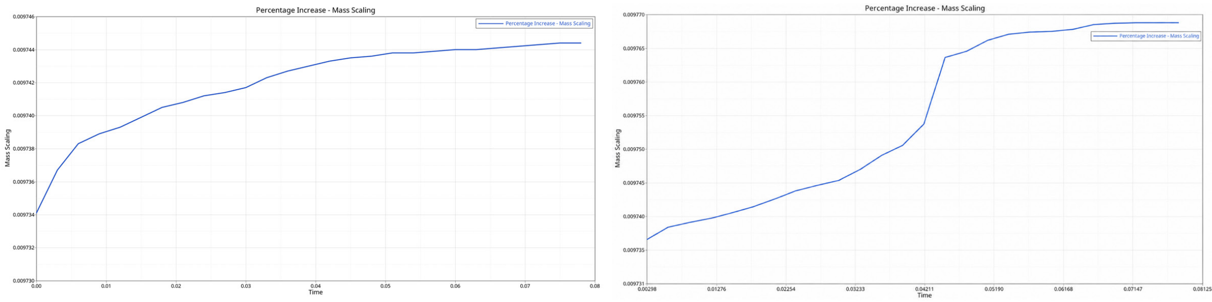

(a) 25 m/min condition

(b) 35 m/min condition

Figure 5. Mass-scaling histories for both conditions.

The velocity histories are shown in **Figure 6**. The velocity reaches zero at approximately 47 ms in the low-speed case and then reverses. In the high-speed case, the zero-velocity point is delayed to approximately 61 ms. The higher initial speed therefore requires a longer contact interval for energy conversion and subjects the impact end to a longer period of elevated loading.

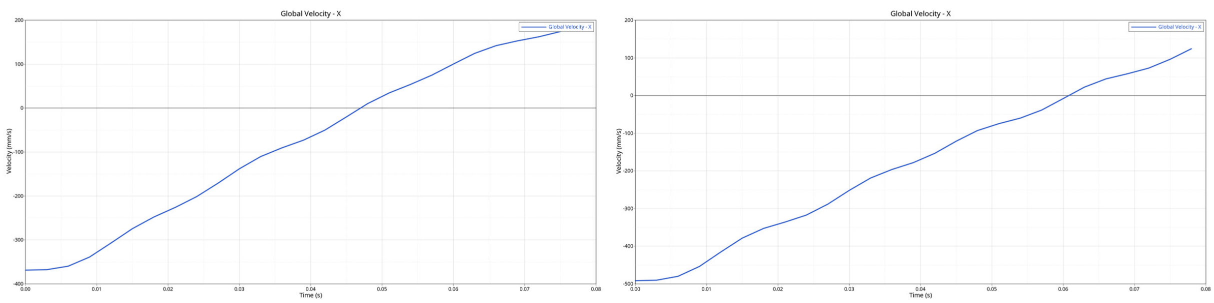

(a) 25 m/min condition

(b) 35 m/min condition

Figure 6. X-velocity histories for both conditions.

4.2. Stress response and yield assessment

The global stress contours in **Figure 7** show that the high-stress region remains concentrated at the impacted end, whereas most of the remote girders and columns stay at low stress. The impact first establishes a local load-transfer zone and then decays along the bridge. Neither speed produces a high-stress field over the complete bridge.

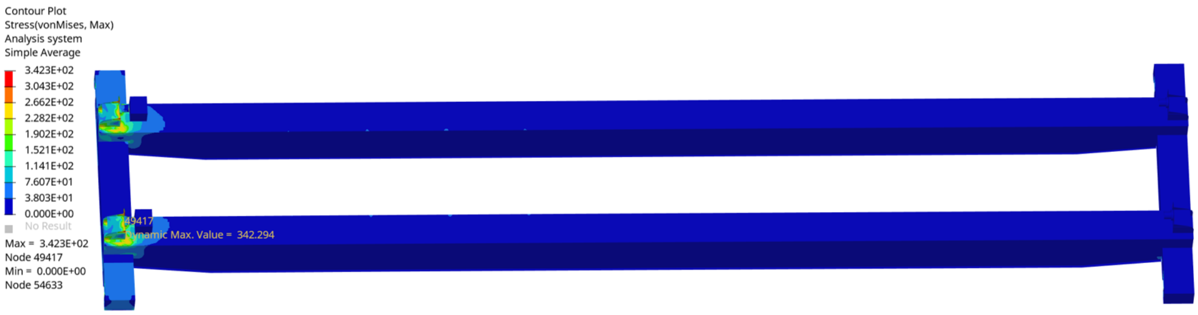

(a) 25 m/min condition

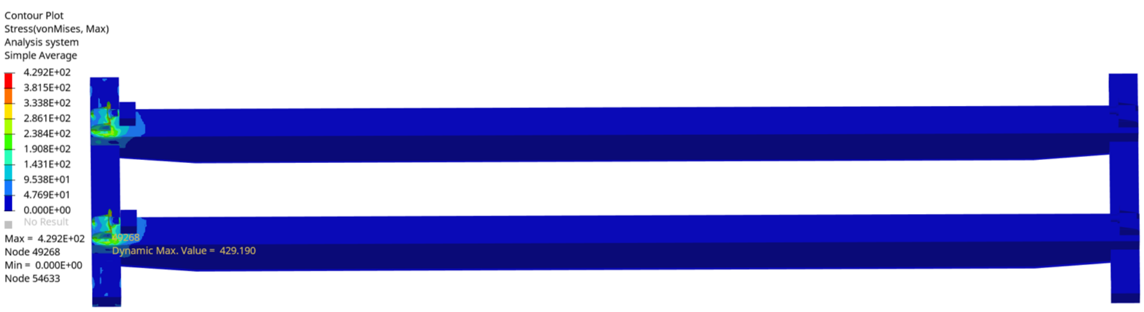

(b) 35 m/min condition

Figure 7. Global von Mises stress contours for both conditions.

The local contours are shown in **Figure 8**. Hu et al. used LS-DYNA to compare steel and CFRP bumper beams under low-velocity impact using energy absorption, peak contact force, and maximum deformation [7]. In the present 25 m/min case, the maximum von Mises stress was 342.294 MPa, which is 2.706 MPa below the 345 MPa yield strength; the corresponding safety factor was approximately 1.008. The mechanism therefore remained nominally below yield, but the small margin could be consumed by manufacturing deviation, weld defects, or repeated impacts.

Marzbanrad et al. compared deflection, impact force, stress distribution, and energy absorption in low-speed frontal crashes and identified material, thickness, shape, and impact condition as key design parameters [8]. In the present 35 m/min case, the peak stress increased to 429.190 MPa, approximately 24.4% above yield, and the safety factor decreased to 0.804. The critical zone occurred in the vertical plate and its neighboring base and support plates, indicating local plasticity in the current load path; relative to the low-speed case, the local strength state therefore changed from near-yield response to above-yield response.

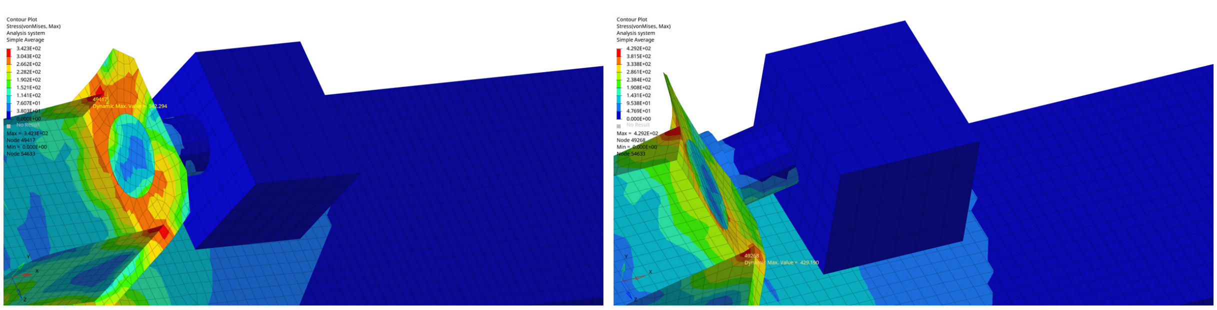

(a) 25 m/min condition (b) 35 m/min condition

Figure 8. Local von Mises stress contours at the impact end.

4.3. Displacement response and condition comparison

Figure 9 presents the X-displacement history of the monitoring node. The maximum displacement was 1.587 mm at 45 ms for 25 m/min and 1.608 mm at 42 ms for 35 m/min. The difference was only 0.021 mm, so peak displacement was relatively insensitive to the velocity change.

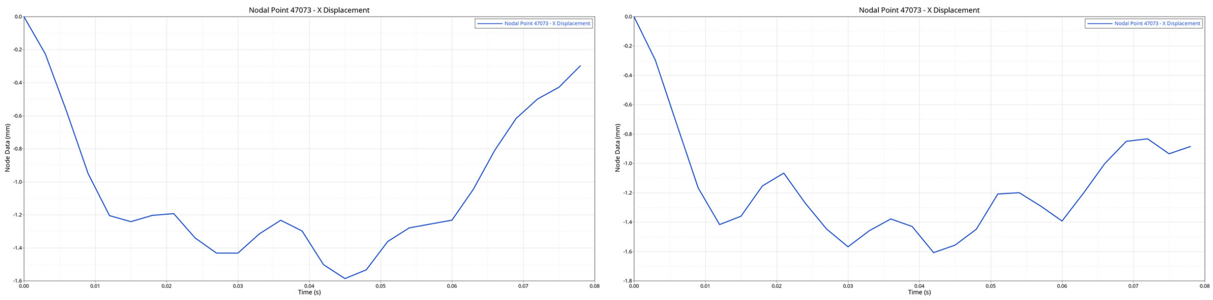

(a) 25 m/min condition (b) 35 m/min condition

Figure 9. X-displacement histories of the monitoring node.

Similar displacement does not imply an equivalent strength state. Global bridge stiffness restricts macroscopic deformation, whereas the local stress concentration is more sensitive to impact speed. Consequently, the high-speed case can exceed yield while total displacement remains small. Tarlochan et al. likewise showed that impact direction and sectional geometry substantially affect the energy absorption and crashworthiness indices of thin-walled absorbers [9]. Engineering assessment should combine energy-quality indices, local stress, and displacement rather than relying on deformation alone. The principal results for both conditions are summarized in **Table 1**.

Table 1. Main simulation results for the two impact conditions

Index	Low-speed condition	High-speed condition
Initial velocity	416.67 mm/s (25 m/min)	583.33 mm/s (35 m/min)
Simulation duration	80 ms	80 ms
Sliding-energy ratio	184,176/3,984,880 mJ = 4.7%	353,179/7,078,580 mJ = 4.9%
Hourglass-energy ratio	7,754/3,984,880 mJ = 0.19%	26,004/7,078,580 mJ = 0.37%
Added mass	0.97%	0.98%
Zero-velocity time	approximately 47 ms	approximately 61 ms
Maximum von Mises stress	342.294 MPa	429.190 MPa
X-displacement at the monitoring point	1.587 mm at 45 ms	1.608 mm at 42 ms
Assessment	Below yield; limited margin	Above yield strength

4.4. Engineering implications

Within the tested range, 25 m/min is an acceptable condition for the existing mechanism, but its limited stress margin does not justify unrestricted operation. The 35 m/min condition is outside the elastic resistance of Q345 steel. In practice, end-zone speed control, limit switches, or obstacle detection should work together with the mechanical device; the passive structure should not be treated as a routine braking component.

If the process requires a higher trolley speed near the end zone, priority should be given to the thickness, fillet geometry, and stiffener orientation around the vertical-plate-to-base connection, together with a replaceable buffer if appropriate. Belingardi et al. evaluated frontal bumper-beam concepts using impact energy, peak load, crash resistance, energy absorption, and stiffness, and emphasized that material, structural design, and manufacturing technology should be considered together [10]. Any modification should therefore balance mass, stiffness, energy absorption, and maintainability.

5. Conclusion

Based on the explicit dynamic results at the two impact speeds, the main conclusions are as follows:

(1) The model maintained satisfactory energy balance at both speeds. Sliding energy, hourglass energy, and added mass remained low, indicating that the response was not governed by obvious numerical artifacts.

(2) Impact speed primarily changed the deceleration history and local strength state. At 25 m/min, velocity reached zero at about 47 ms and the structure remained marginally below yield; at 35 m/min, zero velocity occurred at about 61 ms and the impact end entered a plastic-risk state.

(3) The two peak displacements were nearly identical despite a substantial stress difference. Local equivalent stress, rather than global displacement alone, should therefore be the principal strength index for the mechanism.

(4) The current mechanism should be used together with end-zone speed limitation. If a higher allowable speed is required, local reinforcement around the vertical-plate-to-base connection should be verified by tests or mesh-independent analysis.

6. Limitations and future work

The trolley and lifting assembly were represented by an equivalent rigid body. Weld imperfections, material strain-rate effects, repeated impact, and long-term fatigue were not included, and two speed levels are insufficient to locate the critical speed precisely. Future work should include physical impact testing, mesh-independence and material-sensitivity studies, and additional speed samples between 25 and 35 m/min.

Acknowledgments

The author thanks the supervisor and laboratory members for their assistance with model development and simulation analysis.

Data availability

The finite-element model, response histories, and contour plots were obtained from the author’s bridge-crane anti-collision mechanism project and are available upon reasonable request.

Disclosure statement

The authors declare no conflict of interest.

References

[1] Wang J, Qiang B, He Z, et al., 2019, Sliding Mode Control for Overhead Crane System Based on an Improved Nonlinear Reaching Law. Journal of Ordnance Equipment Engineering, 40(7): 148–152 + 175.

[2] Jiao H, Zhou Q, Li Y, et al., 2015, Structural Model Test of Lightweight Girder of Bridge Crane. Journal of Mechanical Engineering, 51(23): 168–174.

[3] Zhao S, Lin F, Li Y, 2014, Collision-Energy Attenuation Characteristics of an Automotive Energy-Absorbing Bumper. Noise and Vibration Control, 34(6): 102–106.

[4] Belytschko T, Ong J, Liu W, et al., 1984, Hourglass Control in Linear and Nonlinear Problems. Computer Methods in Applied Mechanics and Engineering, 43(3): 251–276.

[5] Hambali A, Sapuan S, Ismail N, et al., 2010, Material Selection of Polymeric Composite Automotive Bumper Beam Using Analytical Hierarchy Process. Journal of Central South University of Technology, 17(2): 244–256.

[6] Olovsson L, Simonsson K, Unosson M, 2005, Selective Mass Scaling for Explicit Finite Element Analyses. International Journal for Numerical Methods in Engineering, 63(10): 1436–1445.

[7] Hu Y, Liu C, Zhang J, et al., 2015, Research on Carbon Fiber-Reinforced Plastic Bumper Beam Subjected to Low-Velocity Frontal Impact. Advances in Mechanical Engineering, 7(6): 1687814015589458.

[8] Marzbanrad J, Alijanpour M, Kiasat M, 2009, Design and Analysis of an Automotive Bumper Beam in Low-Speed Frontal Crashes. Thin-Walled Structures, 47(8–9): 902–911.

[9] Tarlochan F, Samer F, Hamouda A, et al., 2013, Design of Thin Wall Structures for Energy Absorption Applications: Enhancement of Crashworthiness Due to Axial and Oblique Impact Forces. Thin-Walled Structures, 71: 7–17.

[10] Belingardi G, Beyene A, Koricho E, et al., 2015, Alternative Lightweight Materials and Component Manufacturing Technologies for Vehicle Frontal Bumper Beam. Composite Structures, 120: 483–495.